World Scientific
www.worldscientific.com

Insight into Al–Si interface of PERC by Kelvin probe force microscopy

Xingbo Wang*, Guoyu Qian*, Zhou Gao*, Xing Jiang*, Yongji Chen*,
Jian Liu*, Yuan Lin[†,‡,¶] and Feng Pan[*,§,¶]

*School of Advanced Materials
Peking University Shenzhen Graduate School
Shenzhen, 518055, P. R. China

[†]Key Laboratory of Photochemistry
Institute of Chemistry, Chinese Academy of Sciences
Beijing, 100190, P. R. China
[‡]linyuan@iccas.ac.cn
[§]panfeng@pkusz.edu.cn

Passivated emitter and rear cell (PERC) has the advantage of higher short circuit current and open circuit voltage, which are generally claimed to be related to the reduction of rear side recombination and the increase of rear surface reflection. However, few works have focused on exploring the internal conducting mechanism about it. Herein, the influence of PERC technique on improving the short circuit current is investigated by comparing a PERC with a single crystalline silicon (sc-Si) solar cell. The surface potential results measured by Kelvin probe force microscopy show a higher surface potential step at the Al–Si interface of PERC than that of sc-Si cell, indicating a severe energy band variation and a better carrier collecting ability of PERC. Moreover, by using advanced microstructure characterization techniques, the relationship among the surface potential step, morphology and element distribution is fully studied, which proposes a new viewpoint to explain the enhanced performance of PERC.

Keywords: PERC; KPFM; surface potential; back surface field.

In recent years, single crystalline silicon (sc-Si) solar cell has taken a huge amount of the photovoltaic market, owing to the advantages of high efficiency, low cost, good durability and consistency of high-volume production.[1–3] However, with its simple structure of Ag/SiN$_x$/n-Si/p-Si/Al, as shown in Fig. S1 (a), the improvement of photon-to-electron conversion (PCE) efficiency becomes harder and harder. The Passivated Emitter and Rear cell (PERC) structure (Fig. S1(b)) was initially published in 1989 by the University of New South Wales in lab scale.[4] Basically, the PERC has an additional passivation layer in the back between Si and Al electrode compared with normal sc-Si solar cell and the rear contacting scheme of PERC contributes to a reduction of rear surface recombination and an increase of rear surface reflection,[5] which are beneficial to reaching high PCE. So, a further understanding of the chemical composition and electrical performance of the rear Al–Si interface is of great importance to manufacturing Si solar cells with high efficiency. Traditionally, there are several ways to characterize the rear surface of PERC as summarized by the following: (i) testing the minority carrier lifetime, (ii) measuring the surface recombination velocity,[6–8] (iii) using scanning electron microscopy (SEM) and transmission electron microscopy (TEM) to obtain the morphology and microstructure of the interface,[9,10] (iv) utilizing scanning acoustic microscopy (SAM) and light-beam induced current (LBIC) to locate defects underneath the surface.[11] However, all of them can only measure the electrical performance at the Al–Si interface through an indirect route.

Kelvin probe force microscopy (KPFM), an application mode of atomic force microscopy (AFM), can detect the surface potential (SP) of the samples directly with a high resolution at atomic level. As shown in Fig. S2(b), a two-pass scan is carried out in KPFM to detect the SP, during the first pass, a standard tapping mode of AFM is performed to obtain the topography of the sample surface; during the second pass, the tip is lifted up by a certain height and scanned on the basis of the topography profile obtained from the first pass, and both an alternative current (AC) voltage and a direct current (DC) voltage are attached to the tip at the same time, by modulating the DC voltage to eliminate the first-order resonance, the potential of the sample surface can be

¶Corresponding authors.

X. Wang et al.

Table 1. *I–V* performance of samples A and B.

Samples	Type	J_{sc} (mA/cm^2)	V_{oc} (V)	FF (%)	PCE (%)
A	PERC	39.33	0.65	73.30	18.69
B	sc-Si	37.98	0.63	75.60	18.03

calculated.[12] KPFM is first introduced in 1991 by Non-nenmacher *et al.*[13] Since then, KPFM has been widely used as a unique method to characterize electrical properties and SP of material interfaces.[14–19] The SP multiplies *e* (the charge of an electron) corresponds to the vacuum level of an electron, which is defined as the energy of an electron resting at just outside the surface of the solid state device.[20,21] By obtaining the SP of the sample, we can get the information of charge transfer between different layers,[22,23] Fermi energy and work function,[24–26] catalytic activity, reconstruction of surfaces, etc.[12]

In this paper, we investigated the SP of the Al–Si interface of both PERC and sc-Si solar cell by using KPFM, directly obtaining the energy band structure of the cross-section. Compared with SEM and energy dispersive X-ray
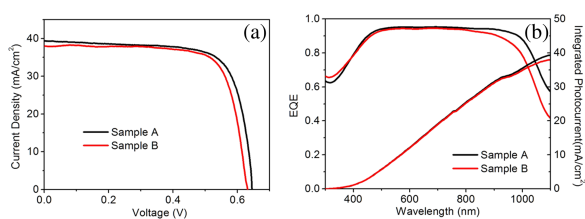
spectroscopy (EDS) results, we found that PERC had a better ability for collecting carriers at the rear side, which was ascribed to a higher surface potential step at the Al–Si interface and the higher doping degree of Al into Si.

In our experiment, we labeled the PERC and sc-Si cell as sample A and sample B, respectively. Their *I–V* performance, including short circuit current density (J_{sc}), open circuit voltage (V_{oc}), fill factor (FF) and PCE, are shown in Table 1 and the current density–voltage ($J-V$) characteristic curves and EQE curves of the two samples are drawn in Figs. 1(a) and 1(b). Their PCEs were 18.69% and 18.03%. Compared with sample B, sample A exhibited a higher V_{oc} and J_{sc}, the higher V_{oc} of PERC was claimed to be related to the reduction of rear side recombination,[27] which weakened the reverse saturation current, and the higher J_{sc} was also claimed to be caused by the reduction of rear side recombination and the enhancement of rear surface reflection,[5] besides, we could see from the EQE result that the higher J_{sc} was mainly attributed to the better EQE performance on the near-infrared side.[28] In fact, the longer the wavelength of light, the smaller the absorption coefficient of silicon.[29] Thus, the better EQE performance on the near-infrared side was attributed to the improvement of the rear side of PERC.

To further explore the internal mechanism of the J_{sc} enhancement of the PERC, we characterized the microstructures of the two samples. After the samples were cut into small pieces and polished by Ar$^+$ ion beams, the cross-section images were observed by SEM and demonstrated in Fig. 2. Figure 2(a) shows the laser ablation dot on the rear side during the fabrication of PERC, the diameter of the dot
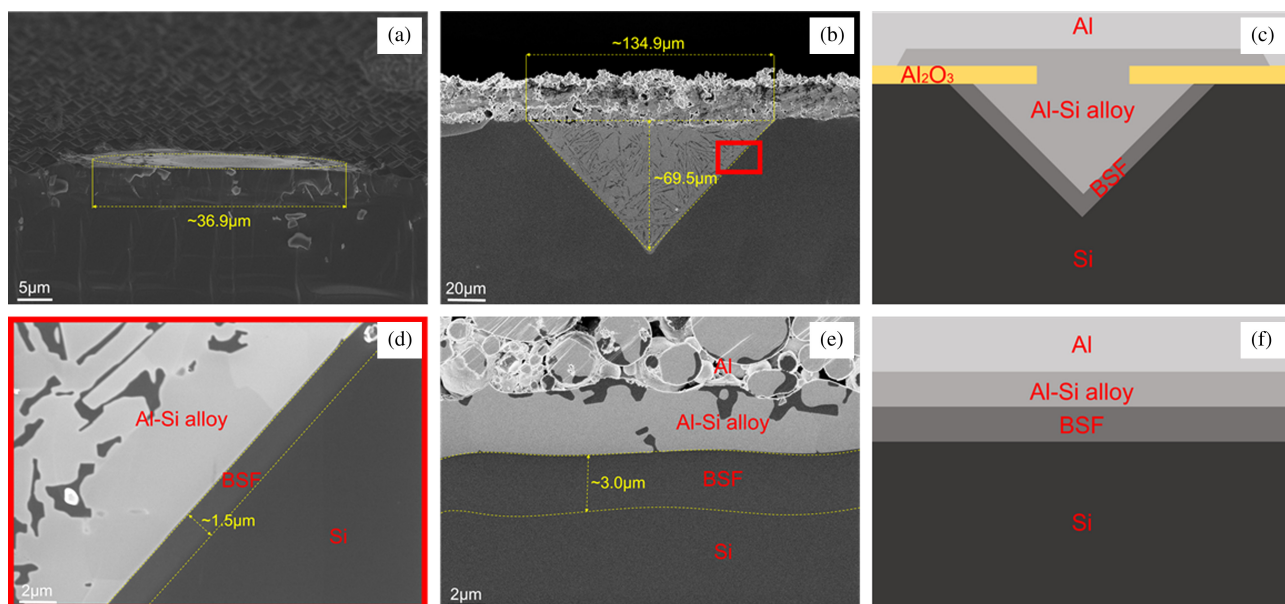

Fig. 1. (a) *J–V* characteristic curves of samples A and B; (b) EQE and integrated photocurrent curves of samples A and B.

Fig. 2. SEM images of cross-sections: (a) Laser ablation dot on the rear side during the fabrication of PERC, (b) rear side of sample A with Al–Si alloy inverted pyramid, (d) and (e) Al–Si interfaces of samples A and B. (c) and (f) Schematic illustrations of the rear side of samples A and B.

was around $37 \mu m$, and the ablation depth was just over $1 \mu m$. After sintering of sample A, the Al–Si alloy part under the ablation dot appeared to be an inverted triangle on the cross-section surface (Fig. 2(b)), but as a matter of fact, it was an inverted pyramid bounded by the Si (111) facets in three-dimensional space.[30] The zoomed morphology images of the Al–Si interfaces of sample A and sample B are shown in Figs. 2(d) and 2(e), the layers with different color contrast represent different chemical components, take Fig. 2(e) for example, those are Al, Al–Si alloy, back surface field (BSF, also known as p+ layer,[12,31,32] caused by the diffusion of Al) and Si, respectively, from the top to the bottom. The inverted pyramid shape of Al–Si alloy of sample A was quite different from that of the sc-Si solar cells, this was because of the limited Al–Si contact area and Si's different dissolution speed into Al for the (111) and (100) facets.[33] Besides, the depth of the Al–Si alloy ($\sim 70 \mu m$) was much larger than that of sample B ($\sim 3.2 \mu m$), but the BSF thickness of sample A ($\sim 1.5 \mu m$) was smaller than that of sample B ($\sim 3.0 \mu m$). Their schematic illustrations are demonstrated in Figs. 2(c) and 2(f). The Al_2O_3 passivation layer between Al and Si at the none-ablated region of sample A is demonstrated in Fig. S3. With the consideration of the shape of inverted pyramid and the interval of laser ablation dots ($500 \mu m$, Fig. S4), the BSF volume per unit area of the back surface could be calculated as around $0.097 \mu m^3/\mu m^2$ for sample A, and $3 \mu m^3/\mu m^2$ for sample B, and the value of sample A accounted for only 3.23% of sample B, indicating a remarkably reduction of Al–Si contact region and the rear side recombination for PERC compared with sc-Si cell. The difference of the morphology lies in the formation of Al–Si alloy and BSF layer during the sintering process, which will be particularly discussed in the last part of this section.

To investigate the electrical property of the region near the Al–Si interface, the SP images were obtained by KPFM under one sun (AM 1.5G) illumination and shown in Figs. 3(a) and 3(b) for samples A and B, respectively. Different colors represent the SP of different layers, take Fig. 3(b) for example, the yellow strip on the left corresponds to the Al–Si alloy, the red strip in the middle corresponds to the BSF layer and the dark brown strip on the right corresponds to the Si bulk. The few dark regions in the Al–Si correspond to Si that recrystallized during the cooling down of sintering.

In order to further analyze the SP variation at the Al–Si interface, the SP profiles along the solid red lines through all the three regions were extracted and illustrated in Figs. 3(c) and 3(d). Actually, the SP data obtained by KPFM was the contact potential difference between tip and sample surface[34] in order to get the absolute potential of the sample surface, the potential of the tip needed to be calibrated, but that was not necessary for our experiment because what we cared
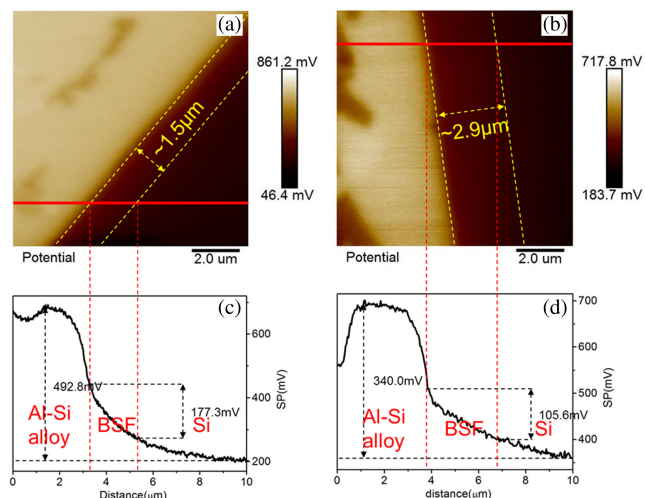

Fig. 3. (a) and (b) SP images of the region near the Al–Si interface of samples A and B tested by KPFM. (c) and (d) SP profiles along the solid red line above of samples A and B.

about here was the SP variation at the interface. As shown in the SP profile image, there was an SP decline from the Al–Si alloy to the Si bulk via the BSF layer, that is, the SPS as we have mentioned above and the SPSs of sample A and sample B were 492.8 mV and 340.0 mV. In addition, the SPS contributed by the BSF layer was demonstrated in Fig. (3) as 177.3 mV and 105.6 mV for samples A and B, combining with the thickness of the BSF layers, we could calculate that the SP gradient in BSF was 117.8 mV/μm for sample A and 35.6 mV/μm for sample B. In fact, when the Al^{3+} ions diffuse into the Si bulk, the p-Si becomes heavily doped p-Si (p+ layer), and the hole density difference between the p-Si and p+ layer forms a hole density gradient driving the holes to move from the p+ layer to the p-Si, generating an inner electric field from the p-Si to the p+ layer, which enhances the collecting of hole carriers generated by illumination. With the existence of the inner electric field, the SP variation becomes larger at the Al–Si interface, thus, the SPS not only reflects the work function variation at the Al–Si interface[35] but also indicates the strength of the inner electric field, the higher the SPS is, the stronger the inner electric field becomes.[12] It results in an improved ability to collect hole carriers for the Al electrode, which leads to a better EQE performance on the near-infrared side for sample A. Therefore, the PERC technique not only reduced the rear side recombination but also enhanced the carrier collecting ability.

In order to understand the origin of the SPS differences between sample A and sample B, the element distribution near the Al–Si interface was carried out by EDS. The zoomed SEM images of the Al–Si interfaces were shown in Figs. 4(a) and 4(b), and the relative element distribution (Al vs Si) profiles along the solid red line were demonstrated in Figs. 4(c) and 4(d). The results showed that the density of Al
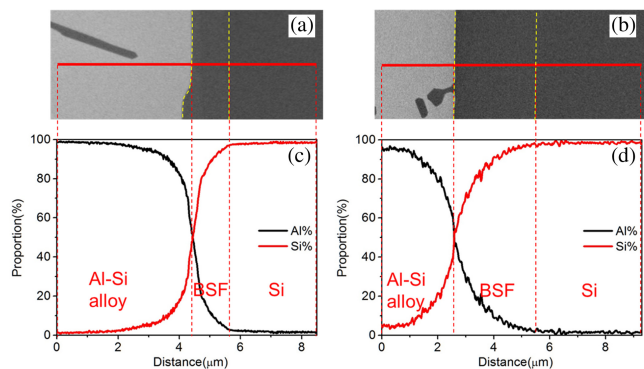
Fig. 4. (a) and (b) Zoomed SEM images of the Al–Si interfaces of samples A and B. (c) and (d) Relative element distribution (Al and Si) profiles along the solid red line above of samples A and B scanned by EDS.

in the Al–Si alloy region and the BSF layer of sample A was higher than that of sample B. Moreover, the element density gradient in the BSF layer of sample A was much higher than that of sample B.

Compared with the sc-Si solar cell (sample B), the PERC (sample A) had a higher SPS, a broader Al-Si alloy region and a thinner BSF layer. The density of Al and its gradient in the BSF layer of sample A were higher than those of sample B. Actually, the sintering process had a great influence on these phenomena mentioned above, we ought to seek the explanation by starting with the melt of Al. According to the Al–Si phase diagram (Fig. S5),[36] when the solar cell was transmitted into the furnace with a peak temperature of $795°C$, the Al started to melt at around $660°C$, forming a melt liquid layer at the Si surface. Meanwhile, the solid Si was dissolved into the Al melt liquid. With the increasing Si content in the generated Al–Si melt liquid, the concentration of Si became nearly saturated, impeding further dissolution of Si. In the process of cooling down, when the phase reached the liquidus, the solid Si was precipitated from the Al–Si melt mixture, and recrystallized epitaxially on the Si bulk surface with Al incorporated into the lattice, forming the BSF layer. When the temperature dropped to $577°C$ (eutectic temperature of Al and Si), the remaining melt liquid started to solidify, generating the Al–Si alloy layer.[37] As the original Al–Si contact area was much more concentrated for the PERC (around 0.43% compared with the sc-Si cell), for each opening region by the laser ablation, the Si had much wider space to diffuse, resulting in a pretty low Si density near the solid–liquid boundary, which led to a higher density and gradient of Al in the BSF layer. It facilitated the intense p+ doping of Al, which would enhance the inner electric field, and finally improved the SPS between Al and Si. On the other hand, the diffusion process of Si had been accelerated significantly due to the lower concentration of Si in Al–Si melt liquid, thus caused a broader Al–Si alloy region after eutectic process. Since the thickness of BSF layer is closely related to the vertical distance between the liquidus temperature and eutectic line (Fig. S5),[36,37] when the temperature went down, the liquidus temperature of Al–Si mixture in the PERC was lower than that in sc-Si cell due to the lower Si density near the solid–liquid boundary, resulting in a thinner BSF layer. Therefore, we can infer that one route to manufacture better rear surface of PERC is to optimize the sintering condition to obtain better BSF layer, the other route is to locally heavily dope the back contact region, enhancing the inner electric field between Al and Si, which has been verified to be feasible by the PERL (passivated emitter and rear locally-diffused) structure,[38,39] and another route is to adjust the Al paste used for PERC or add metallization barriers to limit the dissolution and penetration of Si into Al, which has also been attempted by other researchers.[30,31]

In conclusion, the IV performance showed that PERC had a higher V_{oc} and J_{sc} over sc-Si solar cell; to further explore the internal mechanism of the J_{sc} improvement, their Al–Si interface SP profiles were demonstrated by KPFM. As a result, an SP drop from the Al–Si alloy to the Si bulk had been observed, and the SPS of PERC was higher than that of sc-Si solar cell, indicating a better ability of collecting hole carriers. Combined with the results of SEM and EDS, we found that the main reason for the higher SPS of PERC was attributed to the higher Al density in the Al–Si alloy and BSF layer, which was related to the dissolution, penetration and recrystallization of Si. Therefore, the reasons for the J_{sc} enhancement by PERC technique can be summarized as (i) reduced carrier recombination of the rear side, (ii) increased reflection of the rear surface, and (iii) improved carrier collecting ability of rear side. Clarifying these mechanisms would be beneficial to the high-performance PERC in practical production.

Acknowledgments

References

1. C. Zhang *et al.*, *Nanoscale Res. Lett.* **1**, 13 (2018).
2. Y. Liu *et al.*, *Sol. Energy Mater. Sol. Cells* 140 (2015).
3. N. S. Lewis, *Science* **6271**, 351 (2016).
4. A. W. Blakers, *et al.*, *Appl. Phys. Lett.* **13**, 55 (1989).
5. M. A. Green, *Sol. Energy Mater. Sol. Cells* 143 (2015).
6. H. Huang *et al.*, *Sol. Energy Mater. Sol. Cells* 161 (2017).
7. J. Schmidt *et al.*, Progress in the surface passivation of silicon solar cells, *23rd European Photovoltaic Solar Energy Conference* (2008), pp. 974–981.

8. B. Hoex *et al.*, *J. Appl. Phys.* **4**, 104 (2008).
9. G. Dingemans and W. M. M. Kessels, *J. Vac. Sci. Technol. A* **4**, 30 (2012).
10. H. Si *et al.*, *Nano Energy* 22 (2016).
11. S. Großer *et al.*, *Energy Procedia* 92 (2016).
12. Y.-J. Chen *et al.*, *Nano Energy* 36 (2017).
13. M. Nonnenmacher *et al.*, *Appl. Phys. Lett.* **25**, 58 (1991).
14. C. S. Jiang *et al.*, *Ultramicroscopy* **8**, 109 (2009).
15. M. Tanimoto, *J. Vac. Sci. Technol.* **2**, 14 (1996).
16. Q. Chen *et al.*, *Nat. Commun.* 6 (2015).
17. M. Moczala *et al.*, *Ultramicroscopy* 141 (2014).
18. M. J. Zhang *et al.*, *Nano Lett.* **2**, 16 (2016).
19. Z. Kang *et al.*, *Sci. China Mater.* **6**, 62 (2019).
20. D. Cahen and A. Kahn, *Adv. Mater.* **4**, 15 (2003).
21. H. Ishii *et al.*, *Adv. Mater.* **8**, 11 (1999).
22. L. Fei *et al.*, Investigation of charge transfer in nanostructured hybrid solar cell using Kelvin Probe Force Microscopy, *IEEE 39th Photovoltaic Specialists Conference* (2013), pp. 681–684.
23. M. Konecny *et al.*, *ACS Appl. Mater. Interfaces* **14**, 10 (2018).
24. T. Glatzel *et al.*, *Appl. Phys. Lett.* **11**, 81 (2002).
25. H. Hoppe *et al.*, *Nano. Lett.* **5**, (2005).
26. H. Si *et al.*, *Adv. Funct. Mater.* **30**, 27 (2017).
27. M. A. Green *et al.*, *Appl. Phys. Lett.* **12**, 44 (1984).
28. S. Park *et al.*, *Curr. Appl. Phys.* **9**, 16 (2016).
29. K. Rajkanan *et al.*, *Solid-State Electron.* **9**, 22 (1979).
30. A. Urueña *et al.*, Controlling the depth of the local Al BSF in PERC crystalline solar cells using alternative back side metallization, *25th European Photovoltaic Solar Energy Conference* (2010), pp. 2562–2564.
31. A. Uruena *et al.*, *Energy Procedia* 27 (2012).
32. S. Park *et al.*, *Prog. Photovoltaics* **8**, 22 (2014).
33. A. Uruena *et al.*, Local Al-alloyed contacts for next generation Si solar cells, *24th European Photovoltaic Solar Energy Conference* (2009), pp. 1483–1496.
34. H. O. Jacobs *et al.*, *Rev. Sci. Instrum.* **3**, 70 (1999).
35. C. Scales and P. Berini, *IEEE J. Quantum Electron.* **5**, 46 (2010).
36. J. L. Murray and A. J. McAlister, *Bull. Alloy Phase Diagr.* **1**, 5 (1984).
37. F. Huster, Investigation of the alloying process of screen printed aluminum pastes for the BSF formation on silicon solar cells, *20th European Photovoltaic Solar Energy Conference* (2005), pp. 1466–1469.
38. J. Zhao *et al.*, 24% efficient PERL structure silicon solar cells, *IEEE Photovoltaic Specialists Conference* (1990), pp. 333–335.
39. M. A. Green, *Prog. Photovoltaics* **3**, 17 (2009).